

**Sign inversion in the terahertz photoconductivity of single-walled carbon nanotube films**Peter Karlsen,<sup>1,\*</sup> Mikhail V. Shuba,<sup>2,3,†</sup> Polina P. Kuzhir,<sup>2,3</sup> Albert G. Nasibulin,<sup>4,5</sup> Patrizia Lamberti,<sup>6</sup> and Euan Hendry<sup>1,‡</sup><sup>1</sup>*School of Physics, University of Exeter, Stocker Road, EX4 4QL, United Kingdom*<sup>2</sup>*Institute for Nuclear Problems, Belarus State University, Bobruiskaya 11, 220050 Minsk, Belarus*<sup>3</sup>*Tomsk State University, Lenin Avenue 36, 634050, Tomsk, Russia*<sup>4</sup>*Skolkovo Institute of Science and Technology, Skolkovo Innovation Center, Building 3, Moscow 143026, Russia*<sup>5</sup>*Department of Applied Physics, Aalto University, School of Science, P.O. Box 15100, FI-00076 Espoo, Finland*<sup>6</sup>*Department of Information and Electrical Engineering and Applied Mathematics, University of Salerno, Fisciano (SA), Italy*

(Received 10 January 2018; revised manuscript received 12 October 2018; published 3 December 2018)

In recent years, there have been conflicting reports regarding the ultrafast photoconductive response of films of single walled carbon nanotubes (CNTs), which apparently exhibit photoconductivities that can differ even in sign. Here, we observe explicitly that the THz photoconductivity of CNT films is a highly variable quantity which correlates with the length of the CNTs, while the chirality distribution has little influence. Moreover, by comparing the photoinduced change in THz conductivity with heat-induced changes, we show that both occur primarily due to heat-generated modification of the Drude electron relaxation rate, resulting in a broadening of the plasmonic resonance present in finite-length metallic and doped semiconducting CNTs. This clarifies the nature of the photoresponse of CNT films and demonstrates the need to carefully consider the geometry of the CNTs, specifically the length, when considering them for application in optoelectronic devices.

DOI: [10.1103/PhysRevB.98.241404](https://doi.org/10.1103/PhysRevB.98.241404)

The optical and electronic properties of single-walled carbon nanotubes (CNTs) have been intensely investigated for several decades due to their fascinating physical properties and potential for advanced applications [1–5]. Understanding the ultrafast dynamics of photoexcited charge carriers in CNTs is critical due to their potential applications in photonics and optoelectronics [6–11]. For this reason, many groups have utilized time-resolved measurements to study the ultrafast response of CNTs due to optical photoexcitation, documenting, for example, the presence of excitons in photoexcited CNTs [12–17].

While visible pulses can detect the presence of excitons, terahertz (THz) pulses are ideal for probing low-energy excitations such as free carriers and plasmons, since each of these species have distinct features in the THz photoconductivity [18]. Thus a proper understanding of the THz response of CNTs is key to understanding the ultrafast charge-carrier mechanisms in CNTs. Many groups have utilized optical pump–THz probe time-domain spectroscopy to investigate the ultrafast charge-carrier dynamics in CNTs [16,19–23]; however, there are conflicting reports of the sign and frequency dependence of the observed photoconductivity. This discrepancy has led to wildly different interpretations and conclusions about the photoinduced THz response. For example, Xu *et al.* [19] deduced that excitons are the dominant photogenerated species detected in these experiments, while Luo *et al.* [16] concluded the ultrafast THz response originates from transitions between exciton states. Beard *et al.*

[21] and, more recently Jensen *et al.* [23], have meanwhile concluded that free carriers are the dominant photoexcited species, an interpretation broadly shared by Kampfrath *et al.* [20,22], with small-gap interband transitions also contributing to the THz response. While most of these measurements have been carried out on samples of mixed chirality (i.e., mixed semiconducting and metallic CNTs) it is important to note that Beard *et al.* [21] found THz photoconductivities of samples containing 94% semiconducting and 93% metallic CNTs to be similar. Moreover, discrepancies persist even for nominally similar samples, with Luo *et al.* [16] and Xu *et al.* [19] reporting a photoconductivity of different sign for samples of predominately small-diameter semiconducting CNTs.

Since all of these groups have measured CNTs under similar excitation and preparation conditions, these discrepancies must originate from a difference in the measured samples themselves. The key to understanding these discrepancies lies in the observation of a broad peak in the THz conductivity of CNTs, observed for the first time, to our knowledge, in Ref. [24]. While there has been some discussion regarding the nature of this resonance, with some groups proposing an interband transition of small-gap CNTs [20,25–27], more recent papers [28–31] show clear evidence that it results from a localized plasmon in finite-length CNTs, which we denote the *finite-length effect*, first proposed in Refs. [32,33]. Theoretical modeling [34] and experimental observations [28–31] substantiates the dominant role of the finite-length effect in the equilibrium THz response. Understanding the true origin of this THz resonance is also key to understanding the ultrafast charge-carrier dynamics of CNTs. However, due to the inherent difficulty in fabricating isolated CNT samples, most measurements have been carried out on mixtures of CNTs with various distributions in length, thickness, chirality,

\*peterkarlsen88@gmail.com

†mikhail.shuba@gmail.com

‡E.Hendry@exeter.ac.uk

TABLE I. Summary of our CNT films; thickness ( $D$ ), length ( $L$ ) (average length in parenthesis), diameter ( $d$ ), and content of semiconducting (sem.) and metallic (met.) CNTs. Note that  $l$ -,  $m$ -, and  $s$ -CNT is short notation for *long*-, *medium*-, and *short*-CNT, respectively.

Sample	$D$ (nm)	$L$ ( $\mu\text{m}$ )	$d$ (nm)	sem.	met.
sem-CNT	500	0.1–1	0.8–1.2	99%	1%
met-CNT	500	0.1–1	0.8–1.2	5%	95%
$l$ -CNT	55	2–100 (10)	1.3–2	66%	33%
$m$ -CNT	500	0.3–2 (1)	0.8–1.2	66%	33%
$s$ -CNT	800	<0.3	0.8–1.2	66%	33%

and bundle size, all fabricated using a variety of techniques [19–21,28,34–36].

In this paper, we use optical pump–THz probe time-domain spectroscopy to systematically investigate the influence of tube length and chirality on the THz photoconductivity of thin films comprising single-walled CNTs. We observe explicitly that the THz photoconductivity of CNT films is a highly variable quantity which correlates with the length of the CNTs, while the chirality distribution (i.e., the relative concentration of metallic versus semiconducting tubes) has very little influence. Moreover, by comparing the photoinduced change in THz conductivity ( $\Delta\sigma_{ph}$ ) to the change on heating from 10 to 300 K ( $\Delta\sigma_{heat}$ ), we show that both occur primarily due to the temperature-induced modification of Drude electron relaxation rate, which results in a broadening of the plasmonic resonance present in finite-length metallic and doped semiconducting CNTs.

To study the influence of tube length and chirality, we prepared five types of films comprising CNTs in bundled form, where the average lengths of the CNT bundles and the chirality distributions of the films vary significantly, see Table I. The details of the sample preparation can be found in Sec. S1 in Ref. [37].

In order to observe the influence of the broad THz peak on the photoconductivity of CNTs, it is important to probe at or below the resonance frequency, which typically lies in the range 1–10 THz [28]. We carried out both transmission and photoconductivity measurements over the range 0.2–1.5 THz, where THz pulses were incident normal to our samples. Transmission spectra were obtained using a simple time-domain spectrometer, where THz pulses were generated and detected by commercially available Photoconductive Antennas (PCAs) [38] from *Batop* using a 40-MHz, 1064-nm, femtosecond fibre-laser from *Ekspla*. To investigate the photoexcited THz response of our samples, we employed a 100-fs, 1050-Hz repetition rate, 800-nm Ti:sapphire amplified laser, where THz pulses were generated and detected by optical rectification [39] and electro-optic sampling [40], respectively, in 1-mm-thick ZnTe crystals. To photoexcite the sample, we again use 800 nm pulses, with fluences in the range of 0.7–15  $\mu\text{J}/\text{cm}^2$ . By analyzing the frequency-dependent transmission amplitude and phase of a sample (see Sec. S2 in Ref. [37]), we can determine its complex equilibrium effective conductivity,  $\sigma(\nu)$ , as in Refs. [19,21,29], where  $\nu$  is the frequency. Similarly, by recording the difference in transmission,

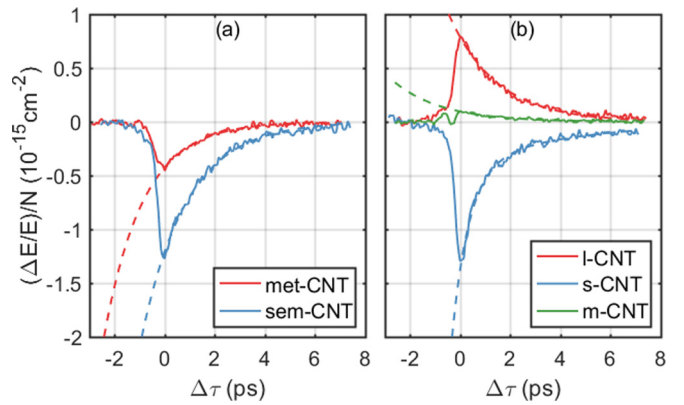


FIG. 1. The photoinduced relative change in the THz transmission  $\Delta E/E$  due to the 800-nm photoexcitation at 300 K of (a) met- and sem-CNT and (b)  $l$ -,  $m$ -, and  $s$ -CNT vs pump-probe delay time  $\Delta\tau$  and normalized by the absorbed photon density  $N$ . The incident fluence is 15  $\mu\text{J}/\text{cm}^2$  for all films except  $l$ -CNT, where the fluence is 0.7  $\mu\text{J}/\text{cm}^2$ . The full lines are the experimentally obtained data, and the dashed lines are exponential fits. The decay time  $\tau$  is found to be 1.8, 1.6, 1.9, and 1.9 ps for sem-, met-,  $l$ -, and  $m$ -CNT, respectively. For  $s$ -CNT, an initial fast decay of 0.7 ps is observed, followed by a slow decay of 4.4 ps.

$\Delta E = E_{exc} - E$ , between a photoexcited ( $E_{exc}$ ) and unexcited sample ( $E$ ), a complex photoconductivity  $\Delta\sigma_{ph}(\nu, \Delta\tau)$  can be obtained as a function of pump-probe delay-time  $\Delta\tau$  (again, see Sec. S2 in Ref. [37]). To investigate the temperature dependence of the THz conductivity in the range 10–300 K, we employed a closed cycle helium cryostat (ARS) [18] with quartz windows. Note that the relatively narrow bandwidth of our measurements is determined by the transmission through this cryostat system and the absorption of our CNT films, see Sec. S2 in Ref. [37] for details. In Fig. (1), we plot the photoinduced change in transmission ( $\Delta E/E$ ) as a function of pump-probe delay time  $\Delta\tau$  and normalized to the absorbed photon density  $N$ , for the met- and sem-CNT (a), and the  $l$ -,  $m$ -, and  $s$ -CNT films (b).<sup>1</sup> We note that the 800-nm photoexcitation occurs primarily off-resonance in terms of the optical transitions in the CNTs, meaning the only on-resonance photoexcitation occurs for a small subset of the semiconducting CNTs in the  $s$ - and  $m$ -CNTs, see Sec. S3 in Ref. [37]. We observe that the decay dynamics of all the films are quite similar, with decay times in the range of 1.6–1.9 ps, comparable to previous reports [19,22,23,41,42], which has previously been attributed to Auger recombination of the photoexcited electron-hole pairs [19,42]. Since we observe little fluence dependence in the decay times of the various CNT films (see Sec. S3 in Ref. [37]), we rule out Auger recombination as a significant relaxation mechanism for our films. Instead, we associate the THz photoresponse and decay

<sup>1</sup>Note that in order to facilitate comparison of photoconductivities of similar order, the incident fluence used for the  $l$ -CNT is two orders of magnitude smaller than for the other samples, due to the relatively large photoresponse of  $l$ -CNT (however, the dynamics and conductivity spectra are observed to be relatively fluence independent for our samples, see Sec. S3 in Ref. [37]).

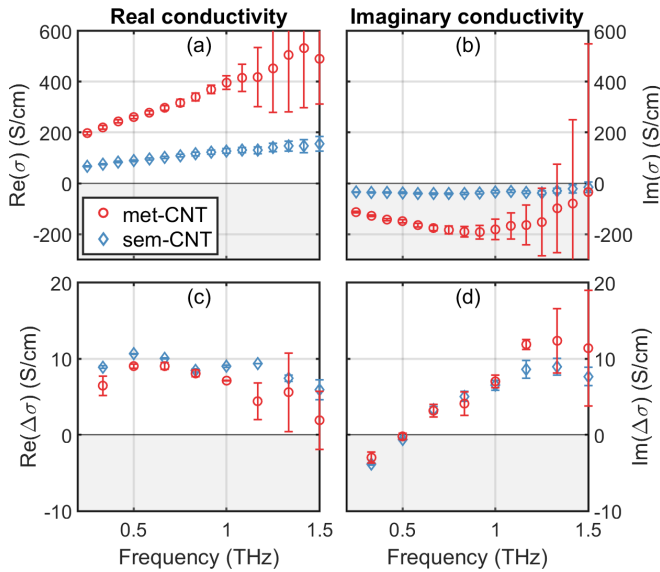


FIG. 2. Effective conductivity (a)  $\text{Re}(\sigma)$  and (b)  $\text{Im}(\sigma)$  of met- and sem-CNT at 300 K, and change in effective conductivity (c)  $\text{Re}(\Delta\sigma)$  and (d)  $\text{Im}(\Delta\sigma)$  due to 800-nm photoexcitation at pump-probe delay time  $\Delta\tau = 1$  ps. The incident fluence is  $15 \mu\text{J}/\text{cm}^2$ . The frequency spacing of the data points correspond to the Nyquist limit of the measurements, and the error bars indicate the standard deviation of each data point. The negative region of the second axis in (a)–(d) have been shaded to highlight the difference in sign of  $\sigma$  and  $\Delta\sigma$ .

times with cooling of the CNT electronic system and lattice, which will become evident later on. While the decay dynamics of the different films are similar, the magnitude of  $\Delta E/E$  varies significantly between the samples, and even changes sign. It is the origin of this large variation in photoresponse that forms the basis of this paper.<sup>2</sup>

In Figs. 2(a) and 2(b), we plot the real and imaginary parts of  $\sigma(\nu)$  for the predominantly semiconducting (sem-CNT) and metallic (met-CNT) films, extracted following section S2 in Ref. [37]. The films show similar conductivities in terms of frequency dependence and sign, resulting from driven oscillation of the plasmon resonance at higher frequency [28,29]. We observe a factor of three difference in conductivity between sem-CNTs and met-CNTs due to the higher free charge density in metallic tubes. However, the frequency of the plasmon resonance is not expected to depend on the density of free charges [43]. When we photoexcite the films away from the optical resonances, we see that the similarity in the responses persists, as previously reported by Beard *et al.* [21]; in Fig. 2(a), we plot the photoconductivity of each film,  $\Delta\sigma_{ph}$ , measured 1 ps after excitation ( $\Delta\tau = 1$  ps). This similarity suggests that the variation in ultrafast CNT photoconductivities reported in the literature [16,19–23] is not

directly linked to a variation in the chirality distribution of the samples.

We therefore move on to consider influence of nanotube length, where we compare the *l*-, *m*- and *s*-CNT films in Fig. 3, defined by average lengths 10, 1, and  $<0.3 \mu\text{m}$ , respectively. Here, we see a drastic difference in the real and imaginary parts of  $\sigma(\nu)$ . For *l*-CNT, we observe a typical free electron (Drude) response (dashed line), indicating that, in this sample, the carriers are free to move along the tube length. However, the *m*- and *s*-CNTs both display a typical plasmonic resonance, located above 1.5 THz, due to the finite-length effect [28,34,44]. Broadband infrared conductivity measurements of these CNT films confirm that the THz resonance shifts to higher frequencies with decreasing tube length [44]. Likewise, the photoinduced THz response is quite variable for these samples of different length CNTs, plotted in Figs. 3(c) and 3(d). For short tubes (*s*-CNT), we observe a photoconductivity  $\Delta\sigma_{ph}$ , measured at  $\Delta\tau = 1$  ps, which has a positive real component and a negative imaginary component for all frequencies in our range. The medium length tubes (*m*-CNT) display a real component of photoconductivity, which changes sign at approximately 0.7 THz, while the longest tubes (*l*-CNT) display a real component of the photoconductivity which is negative for all frequencies in our range. It is interesting to note that the photoconductivity observed for the *l*-CNT film is similar to that observed in the literature by Xu *et al.* [19], and the *m*-CNT is similar to the observation by Kampfrath *et al.* [20], while the behavior of films *s*-, sem-, and met-CNT is similar to that observed by Beard *et al.* and Jensen *et al.* [21,23]. Thus the photoconductivities observed for our films extend across the full range of photoresponses observed previously in the literature.

After illumination with a femtosecond optical stimulus, the electron temperatures in CNTs are thought to rise by several hundred Kelvin [45,46], and the heating of electron and phonon systems occurs even at low pulse fluence, e.g.,  $5 \mu\text{J}/\text{cm}^2$ , as shown for graphite film in [47]. Therefore, to elucidate the origin of this rather peculiar variation in behavior, we also investigate the change in conductivity on heating our samples. In Figs. 3(e)–3(h), we compare  $\Delta\sigma_{ph}$  to the change induced by heating from 10 to 300 K ( $\Delta\sigma_{heat}$ ). The similarity in the change in the frequency response for heating compared to photoexcitation is striking [with the exception of  $\text{Im}(\Delta\sigma)$  for *s*-CNT, discussed below]. Very similar behavior is also observed for the sem- and met-CNT films, shown in Sec. S3 in Ref. [37]. Our observations suggest that  $\Delta\sigma_{ph}$  and  $\Delta\sigma_{heat}$  likely originate from the same underlying mechanism, one that is related to heating induced changes in the conductivity. We note that the intrinsic terahertz conductivity of metallic CNTs with diameters less than 2 nm follows the Drude law, where the plasma frequency does not depend on the temperature (see Ref. [48], Eq. (24)). A dominant heating effect may arise from electron scattering by hot optical phonons [47] as well as acoustical phonons, which have a linear temperature dependence of the Drude scattering rate in CNTs below 500 K [44,49]. However, the influence that this has on the THz conductivity will depend on the frequency and oscillator strength of the THz plasmon resonance. In general, one would expect heating to induce a broadening of the THz peak. However, depending on the frequency of the

<sup>2</sup>The initial oscillatory behavior of the *m*-CNT film is difficult to interpret, since it occurs on a subpicosecond timescale, meaning it could very likely be an artefact from our measurement technique [50].

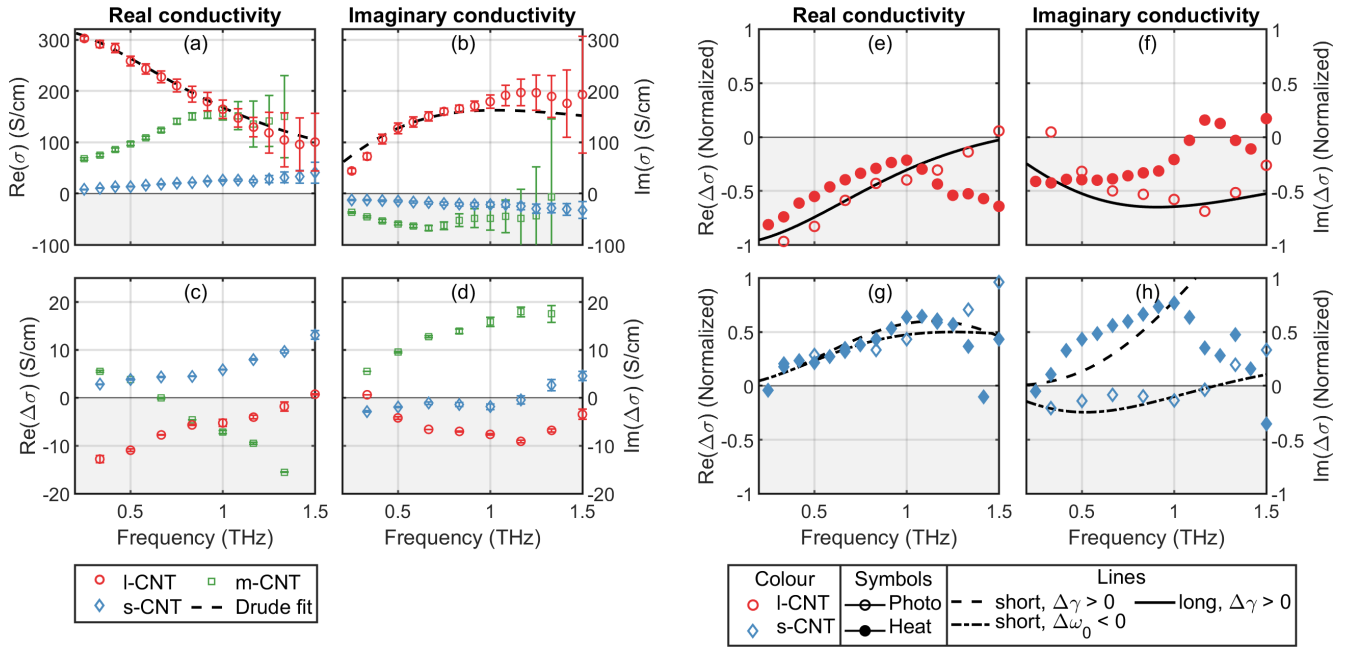


FIG. 3. Effective conductivity (a)  $\text{Re}(\sigma)$  and (b)  $\text{Im}(\sigma)$  of  $l$ -,  $m$ -, and  $s$ -CNT at 300 K, as well as a Drude fit of the  $l$ -CNT, and change in effective conductivity (c)  $\text{Re}(\Delta\sigma)$  and (d)  $\text{Im}(\Delta\sigma)$  due to 800-nm photoexcitation at pump-probe delay time  $\Delta\tau = 1$  ps. The incident fluence is  $0.7 \mu\text{J}/\text{cm}^2$  for  $l$ -CNT and  $15 \mu\text{J}/\text{cm}^2$  for  $s$ - and  $m$ -CNTs. Note that the values of  $l$ -CNT have been scaled by  $10^{-1}$  in (a)–(d). The frequency spacing of the data points correspond to the Nyquist limit of the measurements, and the error bars indicate the standard deviation of each data point. Change in effective conductivity [ $\text{Re}(\Delta\sigma)$  and  $\text{Im}(\Delta\sigma)$ ] of (e) and (f)  $l$ -CNT and (g) and (h)  $s$ -CNT due to heating from 10–300 K (filled symbols), compared with the same  $\Delta\sigma_{ph}$  data as in (c) and (d) (open symbols). Additionally, the black lines in (e)–(h) show the fitted change in conductivity for three simple Lorentzian resonances at resonance frequency  $\omega_0 = 2\pi \times 10^{-2}$  (*long*, full line),  $2\pi \times 10$  (*short*, dashed line), and  $2\pi \times 8$  THz (*short*, dash-dotted line), respectively, which have been fitted to  $\Delta\sigma_{ph}$  for  $l$ -CNT and  $\Delta\sigma_{ph}$  and  $\Delta\sigma_{heat}$  for  $s$ -CNT, respectively. These illustrate the difference in  $\Delta\sigma$  when increasing the scattering rate  $\Delta\gamma > 0$  and when decreasing the resonance frequency  $\Delta\omega_0 < 0$ . Here, we have chosen  $\gamma = 2\pi \times 1.5$  and  $2\pi \times 50$  THz, for the *long* and *short* resonances, respectively, and  $\Delta\gamma = 1$  THz and  $\Delta\omega_0 = -1$  THz. Note that all data in (e)–(h) have been normalized by the maximum absolute value of each  $\Delta\sigma$  in the displayed frequency region to make the overall frequency behavior more comparable.

resonance, this can lead to either an increase or decrease of the effective conductivity of the CNT film in the THz range. To illustrate this effect, in Figs. 3(e)–3(h), we fit the differential conductivity expected for a Lorentzian resonator, given by

$$\sigma = -i\omega\epsilon_0 \left( \frac{A}{\omega^2 - \omega_0^2 + i\omega\gamma} \right), \quad (1)$$

where  $A$  is the oscillator strength,  $\epsilon_0 = 8.85 \times 10^{-12} \text{ F m}^{-1}$  is the vacuum permittivity, and  $\gamma$  is the scattering rate. We note that this simple model ignores contributions to the scattering rate from inhomogeneous broadening over CNT length (see Eqs. (1) and (2) in Ref. [34]). The fits give us three Lorentzians with resonance frequencies located at  $\omega_0 = 2\pi \times 10$  and  $2\pi \times 8$  THz, representing  $s$ -CNTs (fitted to  $\Delta\sigma_{ph}$  and  $\Delta\sigma_{heat}$  for  $s$ -CNT, respectively), and  $\omega_0 = 2\pi \times 10^{-2}$  THz, representing  $l$ -CNTs (fitted to  $\Delta\sigma_{ph}$  for  $l$ -CNT). It is straightforward to qualitatively reproduce the general trends of the observed real part of the value  $\Delta\sigma = (\partial\sigma/\partial\gamma)\Delta\gamma$  in Figs. 3(e) and 3(f) by assuming a heat induced increase in the scattering rate,  $\gamma$ . This gives rise to a change in the real part of the conductivity, which is negative for a low-frequency resonator ( $\omega_0 = 2\pi \times 10^{-2}$  THz) and positive for a high-frequency resonator ( $\omega_0 = 2\pi \times 10$  and  $2\pi \times 8$  THz). Based

on this simple consideration, we conclude that both  $\Delta\sigma_{ph}$  and  $\Delta\sigma_{heat}$  are determined predominantly from heat induced changes to electron scattering.

It is interesting to note that the opposite signs of  $\text{Im}(\Delta\sigma_{heat})$  and  $\text{Im}(\Delta\sigma_{ph})$  for  $s$ -CNT below 1.25 THz indicate that thermal heating and photoexcitation bring about slightly different changes to the carrier distribution. In order to reproduce this sign change, we must additionally introduce a small change to the resonance frequency, shifting to lower frequency after photoexcitation [see black dash-dotted line for  $\Delta\sigma = (\partial\sigma/\partial\omega_0)\Delta\omega_0$  in Figs. 3(g) and 3(h)]. The origin of this effect can be understood as follows. In such a percolated CNT network, the plasmon resonance frequency is determined not by the physical length of each tube, but by the effective length of conductivity pathways in the network (see Ref. [44]). On photoexcitation with optical light, some energetic carriers will be able to escape local energy minima, become more delocalized, and increase the average effective length. Such an effect will be most important for short length tubes, as observed in experiment.

In conclusion, using optical pump–THz probe time-domain spectroscopy, we measured the photoinduced change in THz conductivity,  $\Delta\sigma_{ph}$ , in free-standing carbon nanotube (CNT) films of different lengths and chirality distributions. By

comparing CNT films with average individual tube lengths ranging from 0.3 to 10  $\mu\text{m}$ , we demonstrated that drastic variations in  $\Delta\sigma_{ph}$  observed for various films primarily originate from changes to the plasmonic resonance observed in finite length CNTs due to expected heat-induced changes to electron scattering. Thus we conclude that the photoexcited ultrafast THz response is predominately plasmonic in nature, and that the length of the CNTs is what determines the frequency-dependent behavior. This explains the conflicting reports presented in Refs. [16,19–23] and underlines the need to carefully consider the length of the CNTs when analyzing their ultrafast THz response, and more importantly, when developing nanotube-based optoelectronic devices such as photodetectors [10] and ultrafast polarization modulators [11], since the CNT geometry in these devices will have a huge influence on their performance. To this end, we

have also shown OPTP to be a simple and efficient technique for predicting the geometry of CNT films, which currently requires careful statistical measurements with electron microscopy.

This research was partially supported by the European Union's Seventh Framework Programme (FP7) for research, technological development and demonstration under Project No. 607521 NOTEDEV, and by EPSRC fellowship EP/K041215/1. A.G.N. thanks the Russian Science Foundation (Project identifier: 17-19-01787) for supporting the synthesis of carbon nanotubes and film fabrication. P.L., M.V.S., and P.P.K. thank for support H2020 project 696656 Graphene Core1, and for partial support H2020 RISE project 644076 CoExAN and H2020 RISE project 734164 Graphene 3D. P.P.K. and M.V.S. also are thankful for support by Tomsk State University Competitiveness Improvement Program.

- 
- [1] S. Reich, C. Thomsen, and J. Maultzsch, *Carbon Nanotubes: Basic Concepts and Physical Properties* (Wiley, 2008).
- [2] M. Portnoi, O. Kibis, and M. Rosenau da Costa, *Superlattices Microstruct.* **43**, 399 (2008).
- [3] X. He, N. Fujimura, J. M. Lloyd, K. J. Erickson, A. A. Talin, Q. Zhang, W. Gao, Q. Jiang, Y. Kawano, R. H. Hauge, F. Léonard, and J. Kono, *Nano Lett.* **14**, 3953 (2014).
- [4] L. V. Titova, C. L. Pint, Q. Zhang, R. H. Hauge, J. Kono, and F. A. Hegmann, *Nano Lett.* **15**, 3267 (2015).
- [5] A. Zubair, D. E. Tsentalovich, C. C. Young, M. S. Heimbeck, H. O. Everitt, M. Pasquali, and J. Kono, *Appl. Phys. Lett.* **108**, 141107 (2016).
- [6] S. Nanot, E. H. Házor, J.-H. Kim, R. H. Hauge, and J. Kono, *Adv. Mater.* **24**, 4977 (2012).
- [7] P. Avouris, Z. Chen, and V. Perebeinos, *Nat. Nanotech.* **2**, 605 (2007).
- [8] P. Avouris, M. Freitag, and V. Perebeinos, *Nat. Photonics* **2**, 341 (2008).
- [9] L. François, *The Physics of Carbon Nanotube Devices* (William Andrew, 2009), p. 296.
- [10] T.-F. Zhang, Z.-P. Li, J.-Z. Wang, W.-Y. Kong, G.-A. Wu, Y.-Z. Zheng, Y.-W. Zhao, E.-X. Yao, N.-X. Zhuang, and L.-B. Luo, *Sci. Rep.* **6**, 38569 (2016).
- [11] C. J. Docherty, S. D. Stranks, S. N. Habisreutinger, H. J. Joyce, L. M. Herz, R. J. Nicholas, and M. B. Johnston, *J. Appl. Phys.* **115**, 203108 (2014).
- [12] G. Soavi, F. Scotognella, G. Lanzani, and G. Cerullo, *Adv. Opt. Mater.* **4**, 1670 (2016).
- [13] F. Wang, G. Dukovic, L. E. Brus, and T. F. Heinz, *Science* **308**, 838 (2005).
- [14] A. Srivastava, H. Htoon, V. I. Klimov, and J. Kono, *Phys. Rev. Lett.* **101**, 087402 (2008).
- [15] J. Chmeliov, J. Narkeliunas, M. W. Graham, G. R. Fleming, and L. Valkunas, *Nanoscale* **8**, 1618 (2016).
- [16] L. Luo, I. Chatzakis, A. Patz, and J. Wang, *Phys. Rev. Lett.* **114**, 107402 (2015).
- [17] N. O. Haugen, A. B. Phillips, T. E. Dykstra, S. Wathage, M. J. Heben, and R. J. Ellingson, *J. Phys. Chem. C* **118**, 25253 (2014).
- [18] R. Ulbricht, E. Hendry, J. Shan, T. F. Heinz, and M. Bonn, *Rev. Mod. Phys.* **83**, 543 (2011).
- [19] X. Xu, K. Chuang, R. J. Nicholas, M. B. Johnston, and L. M. Herz, *J. Phys. Chem. C* **113**, 18106 (2009).
- [20] T. Kampfrath, K. von Volkman, C. M. Aguirre, P. Desjardins, R. Martel, M. Krenz, C. Frischkorn, M. Wolf, and L. Perfetti, *Phys. Rev. Lett.* **101**, 267403 (2008).
- [21] M. C. Beard, J. L. Blackburn, and M. J. Heben, *Nano Lett.* **8**, 4238 (2008).
- [22] L. Perfetti, T. Kampfrath, F. Schapper, A. Hagen, T. Hertel, C. M. Aguirre, P. Desjardins, R. Martel, C. Frischkorn, and M. Wolf, *Phys. Rev. Lett.* **96**, 027401 (2006).
- [23] S. A. Jensen, R. Ulbricht, A. Narita, X. Feng, K. Müllen, T. Hertel, D. Turchinovich, and M. Bonn, *Nano Lett.* **13**, 5925 (2013).
- [24] F. Bommeli, L. Degiorgi, P. Wachter, W. S. Bacsa, W. A. de Heer, and L. Forro, *Synth. Met.* **86**, 2307 (1997).
- [25] A. Ugawa, A. G. Rinzler, and D. B. Tanner, *Phys. Rev. B* **60**, R11305 (1999).
- [26] F. Borondics, K. Kamarás, M. Nikolou, D. B. Tanner, Z. H. Chen, and A. G. Rinzler, *Phys. Rev. B* **74**, 045431 (2006).
- [27] H. Nishimura, N. Minami, and R. Shimano, *Appl. Phys. Lett.* **91**, 011108 (2007).
- [28] M. V. Shuba, A. G. Paddubskaya, A. O. Plyushch, P. P. Kuzhir, G. Y. Slepian, S. A. Maksimenko, V. K. Ksenovich, P. Buka, D. Seliuta, I. Kasalynas, J. Macutkevicius, G. Valusis, C. Thomsen, and A. Lakhtakia, *Phys. Rev. B* **85**, 165435 (2012).
- [29] Q. Zhang, E. H. Házor, Z. Jin, L. Ren, X. Wang, R. S. Arvidson, A. Lüttge, and J. Kono, *Nano Lett.* **13**, 5991 (2013).
- [30] T. Morimoto, S.-K. Joung, T. Saito, D. N. Futaba, K. Hata, and T. Okazaki, *ACS nano* **8**, 9897 (2014).
- [31] A. L. Falk, K.-C. Chiu, D. B. Farmer, Q. Cao, J. Tersoff, Y.-H. Lee, P. Avouris, and S.-J. Han, *Phys. Rev. Lett.* **118**, 257401 (2017).
- [32] N. Akima, Y. Iwasa, S. Brown, A. Barbour, J. Cao, J. Musfeldt, H. Matsui, N. Toyota, M. Shiraiishi, H. Shimoda, and O. Zhou, *Adv. Mater.* **18**, 1166 (2006).
- [33] G. Y. Slepian, M. V. Shuba, S. A. Maksimenko, and A. Lakhtakia, *Phys. Rev. B* **73**, 195416 (2006).
- [34] G. Y. Slepian, M. V. Shuba, S. A. Maksimenko, C. Thomsen, and A. Lakhtakia, *Phys. Rev. B* **81**, 205423 (2010).
- [35] B. Kim, J. Lee, and I. Yu, *J. Appl. Phys.* **94**, 6724 (2003).

- [36] W. Bauhofer and J. Z. Kovacs, *Compos. Sci. Technol.* **69**, 1486 (2009).
- [37] See Supplemental Material at <http://link.aps.org/supplemental/10.1103/PhysRevB.98.241404> for further information regarding sample preparation, experimental methods and analysis, and additional data sets.
- [38] C. Fattinger and D. Grischkowsky, *Appl. Phys. Lett.* **54**, 490 (1989).
- [39] X. Zhang, Y. Jin, and X. F. Ma, *Appl. Phys. Lett.* **61**, 2764 (1992).
- [40] Q. Wu and X.-C. Zhang, *Appl. Phys. Lett.* **70**, 1784 (1997).
- [41] J.-S. Lauret, C. Voisin, G. Cassabois, C. Delalande, P. Roussignol, O. Jost, and L. Capes, *Phys. Rev. Lett.* **90**, 057404 (2003).
- [42] F. Wang, G. Dukovic, E. Knoesel, L. E. Brus, and T. F. Heinz, *Phys. Rev. B* **70**, 241403 (2004).
- [43] S. Das Sarma and E. H. Hwang, *Phys. Rev. Lett.* **102**, 206412 (2009).
- [44] P. Karlsen, M. Shuba, C. Beckerleg, D. Yuko, P. Kuzhir, S. A. Maksimenko, V. Ksenevich, H. Viet, A. Nasibulin, R. Tenne, and E. Hendry, *J. Phys. D: Appl. Phys.* **51**, 014003 (2017).
- [45] T. Hertel and G. Moos, *Phys. Rev. Lett.* **84**, 5002 (2000).
- [46] G. Moos, R. Fasel, and T. Hertel, *J. Nanosci. Nanotechnol.* **3**, 145 (2002).
- [47] T. Kampfrath, L. Perfetti, F. Schapper, C. Frischkorn, and M. Wolf, *Phys. Rev. Lett.* **95**, 187403 (2005).
- [48] G. Y. Slepyan, S. A. Maksimenko, A. Lakhtakia, O. Yevtushenko, and A. V. Gusakov, *Phys. Rev. B* **60**, 17136 (1999).
- [49] X. Zhou, J.-Y. Park, S. Huang, J. Liu, and P. L. McEuen, *Phys. Rev. Lett.* **95**, 146805 (2005).
- [50] H.-K. Nienhuys and V. Sundström, *Appl. Phys. Lett.* **87**, 012101 (2005).